NEUROSCIENCE

Excessive local host-graft connectivity in aging and amyloid-loaded brain

Judith Thomas[1,2,3], Maria Fernanda Martinez-Reza[1,2,3], Manja Thorwirth[1,2], Yvette Zarb[1,2], Karl-Klaus Conzelmann[4], Stefanie M. Hauck[5]*, Sofia Grade[1,2]*†‡, Magdalena Götz[1,2,6]*‡§

Transplantation is a clinically relevant approach for brain repair, but much remains to be understood about influences of the disease environment on transplant connectivity. To explore the effect of amyloid pathology in Alzheimer's disease (AD) and aging, we examined graft connectivity using monosynaptic rabies virus tracing in APP/PS1 mice and in 16- to 18-month-old wild-type (WT) mice. Transplanted neurons differentiated within 4 weeks and integrated well into the host visual cortex, receiving input from the appropriate brain regions for this area. Unexpectedly, we found a prominent several-fold increase in local inputs, in both amyloid-loaded and aged environments. State-of-the-art deep proteome analysis using mass spectrometry highlights complement system activation as a common denominator of environments promoting excessive local input connectivity. These data therefore reveal the key role of the host pathology in shaping the input connectome, calling for caution in extrapolating results from one pathological condition to another.

INTRODUCTION

There is an urgent medical need for replacement of degenerated neurons after brain injury or neurodegenerative disease (*1*, *2*). Transplantation of fetal or pluripotent stem cell (PSC)–derived neurons is at the forefront of this approach and has successfully achieved clinical improvements (*1–8*). The easier access and scalability of neurons from induced PSCs for transplantation have further boosted the attempts for clinical translation, e.g., in Parkinson's disease (PD) patients (*9–11*). However, rather little is known about neuronal graft integration in other neurodegenerative diseases or physiological aging.

To repair neural circuit structure and function, transplanted neurons must connect properly. Aberrant wiring may perturb adequate circuit function, especially in diseases affecting the cerebral cortex, given its high excitatory drive. While the output connectivity of neuronal transplants was found to be remarkably specific many years ago (*12–17*), the brain-wide analysis of input connectivity and in vivo observation of neuronal activity evoked by stimulation of those afferents or sensory stimulation have been probed more recently (*18–22*). Fetal cells grafted into the cerebral cortex after neuronal ablation receive brain-wide inputs from the host, as revealed by rabies virus (RABV)–based retrograde monosynaptic tracing (*18*). These inputs closely resemble the input connectome of the lost cortical neurons (*18*). Co-registration of RABV-based tracing and three-dimensional (3D) magnetic resonance imaging demonstrated synaptic integration of human neural transplants grafted into different brain regions in mice (*23*). Similar results have been obtained with cells grafted in a stroke model (*20*, *22*), in a traumatic brain injury (TBI) model (*24*), or in PD models (*21*, *25*, *26*), although the brain-wide input connectome was not quantified. Contrary to acute injuries, characterized by two distinct and in some ways counteracting phases, a proinflammatory acute and an anti-inflammatory chronic phase, conditions differ profoundly during aging and in many neurodegenerative diseases, with progressive and slow synapse and neuron loss and steady changes of the environment (*27–29*). Reactive gliosis after acute and invasive brain damage, such as stroke and TBI (*30*, *31*), differs profoundly from that in the aging brain or in Alzheimer's disease (AD) models (*32–35*). Aging or amyloid-loaded AD brains present vastly different host environments, where transplants survive, but their connectivity remains unknown (*36–39*).

Beyond the lack of connectivity analysis of transplants in these highly relevant conditions, basic principles for new neuron integration into a preexisting circuitry are not known. Transplantation into the adult brain has mostly been performed in models with neuronal loss, but little is known if loss of neurons is a prerequisite to integrate new ones. Synaptic loss is often the first step before neurodegeneration, and it is not known if and how it may influence the integration of new neurons into preexisting but degenerating circuits. In addition, the contribution of reactive gliosis and inflammation to host-graft connectivity has been hardly explored. The influence of inflammation is difficult to deduce from previous studies of human cell transplants, as these xenografts require immunosuppression (*20*, *22*, *36*, *40*). To disentangle the influence of these parameters on transplant connectivity, we explored aging and amyloid-loaded brain environments in murine models without loss of neurons but with loss of synapses and a different extent of reactive gliosis (*33*, *35*, *41*).

The aging brain is characterized by gradual cellular and molecular changes like oxidative damage and mitochondrial dysfunction, accumulation of aggregated proteins, and mild inflammation accompanied by mild reactive gliosis (*42–44*). These age-related changes cause synapse loss, which ultimately leads to impaired function and cognitive decline (*42*). In addition, aging is the main risk factor for

neurodegenerative diseases like AD (*45*). Hallmarks of AD include the extracellular accumulation of misfolded amyloid-β peptide fibrils that aggregate forming plaques, also eliciting astro- and microgliosis and loss of synapses, eventually resulting in network dysfunction and cognitive impairments (*46*). Thus, it is important to understand how these environments may affect synaptic integration of transplanted neurons to determine the effect of basic parameters, such as synapse loss and reactive gliosis onto graft integration, as well as to illuminate their clinical relevance.

RESULTS

Characterization of amyloid pathology and aging mouse models

To explore the integration of new neurons into an environment with stronger versus weaker pathology and no neuron loss, we chose mouse models of AD and aging, respectively, and used allografts, allowing us to probe these basic principles while simultaneously exploring graft integration into highly relevant dysfunctional environments. First, we compared the extent of reactive gliosis in both models. The APP/PS1 mouse model of AD used here overexpresses human amyloid precursor protein (APP) and presenilin 1 (PS1) in neurons (*32*) lacking neuronal death in the cerebral cortex (*47*). These transgenic mice develop early cerebral amyloidosis accompanied by the appearance of hypertrophic microglia and reactive astrocytes and show dendritic spine loss around deposited amyloid plaques (*32, 33, 48*). Staining for glial fibrillary acidic protein (GFAP) to label reactive astrocytes and ionized calcium binding adaptor molecule 1 (Iba1) to label microglia showed profound reactive gliosis in the cortex of APP/PS1 transgenic mice at 8 months of age compared to age-matched wild-type (WT) control animals of the same background (C57BL/6J) (see Materials and Methods for details; fig. S1, A and B). For a quantitative readout, we assessed the number and morphology of microglia and length of their processes and found significant changes between the control and the APP/PS1 mice. This confirmed high microglial reactivity, with a significant increase in the number of microglia (fig. S1, D, E, and G), as well as of its activation state, with fewer branches and ramifications in transgenic mice compared to WT controls (fig. S1, D, E, and H to J).

We then analyzed the glial state in aging cerebral cortices of 16- to 18-month-old WT mice of the same background (C57BL/6J) as the AD model. Both GFAP and Iba1 staining revealed much lower reactivity in cortices of WT aged mice compared to APP/PS1 transgenic mice (fig. S1, B and C). Accordingly, our detailed microglia analysis revealed no significant change in Iba1-stained microglia number or their process length and branching in cortices of 8-month-old versus 16- to 18-month-old WT mice (fig. S1, D, F, and G to J). However, a significantly higher percentage of microglial cells have a large volume covered by their processes in the aged compared to control cortices (fig. S1, K to N). Together, this analysis shows lower levels of reactive gliosis in the aged brain compared to the amyloid pathology, making this comparison very interesting, as both models exhibit altered synaptic dynamics (*43, 48, 49*).

New neurons survive and integrate into cortical circuits in APP/PS1 and aged mice

To explore the influence of the distinctive cellular and molecular environments of APP/PS1 and aged brains on synaptic integration of transplanted neurons, we used our previously established paradigm

of cell transplantation, circuit mapping, and quantitative connectomics (*18*). Mouse cortical cells were isolated from embryonic day 14 (E14) C57BL/6J embryos and transduced with a retrovirus encoding the rabies glycoprotein (G), which is required for its retrograde transport, the receptor TVA (avian tumor virus receptor A) allowing for selective infection of these cells by the Env-A-pseudotyped RABV (*50*), and a fluorescent protein (FP; Fig. 1A). After 3 to 5 days in culture, cells were collected and transplanted into the primary visual cortex (V1) of 8-month-old APP/PS1 transgenic mice. At this age, plaque deposition and reactive gliosis are widespread (fig. S1), as is the decrease in dendritic spines in the absence of neuron loss (*32, 47*). As controls, APP/PS1 WT littermates of the same background (C57BL/6J) and C57BL/6J mice, both of the same age, were used. As a third condition, we also transplanted cells into 16- to 18-month-old aging C57BL/6J mice (Fig. 1A). In previous work, we had not found any difference in the input connectome to cells cultured and infected in vitro or acutely dissociated from the cortex of E18 *Emx1Cre/G-TVA/GFP* transgenic mice before transplantation (*18*). To ensure that this is also the case in the host environments tested here, we also performed a few transplantations with acutely dissociated E18 cortical cells (fig. S2G). Analysis at 5 weeks post-transplantation (wpt) showed that donor cells survived well in all three conditions and no difference in graft size and volume was observed (Fig. 1, B to D, and fig. S2, A to E).

To trace the synaptic inputs to transplants developed in all the conditions, we injected EnvA-pseudotyped and G-deleted RABV (*50*) expressing green fluorescent protein (GFP) or mCherry [referred to as red fluorescent protein (RFP)], depending on donor cell fluorescence. This allowed selective targeting of TVA-expressing donor cells at 4 wpt followed by circuit analysis 1 week thereafter (Fig. 1A). We ensured the reliability of the transsynaptic tracing by injecting the modified RABV into V1 of nontransplanted WT mice and by transplanting cells expressing only the TVA receptor and RFP, but no G protein, followed by RABV injection (fig. S3). We only detected double-labeled donor cells (RFP$^+$/GFP$^+$) but no traced presynaptic partners in the aged or APP/PS1 grafted cortices (fig. S3), indicating that the RABV spread is specific to cells expressing the G protein.

We then proceeded with the experimental conditions by transplanting cells expressing TVA and G protein together with an FP. Grafted cells that were infected by the RABV are referred to as starter cells and were present within the graft in all conditions [RFP$^+$/GFP$^+$; Fig. 1, B to D′; for the exact number of starter cells per mouse and condition, see fig. S2 (F and G)]. Transplants were surrounded by GFP$^+$ traced neurons, i.e., input neurons (or RFP$^+$ input neurons, depending on the donor cell type and corresponding RABV), in all three conditions. However, these were substantially higher in number in the cortices of transgenic APP/PS1 and WT aged mice (Fig. 1, B to D). Thus, transplanted neurons survive and integrate into these brain environments in the absence of any prior neuronal loss.

Excessive local connectivity of neuronal grafts in an amyloid plaque–loaded cortex

Next, we quantified the distribution of the traced neurons across the brain and their average distance to the graft core in the visual cortex (Fig. 1, E and F) to control for any changes in long-distance tracing or any unexpected effects in these host environments. Notably, the brain-wide distribution and distance of local traced neurons were indistinguishable between experimental groups (Fig. 1, E and F). We then calculated the brain-wide input connectivity expressed as connectivity ratio (CR) for each and all innervating regions, as
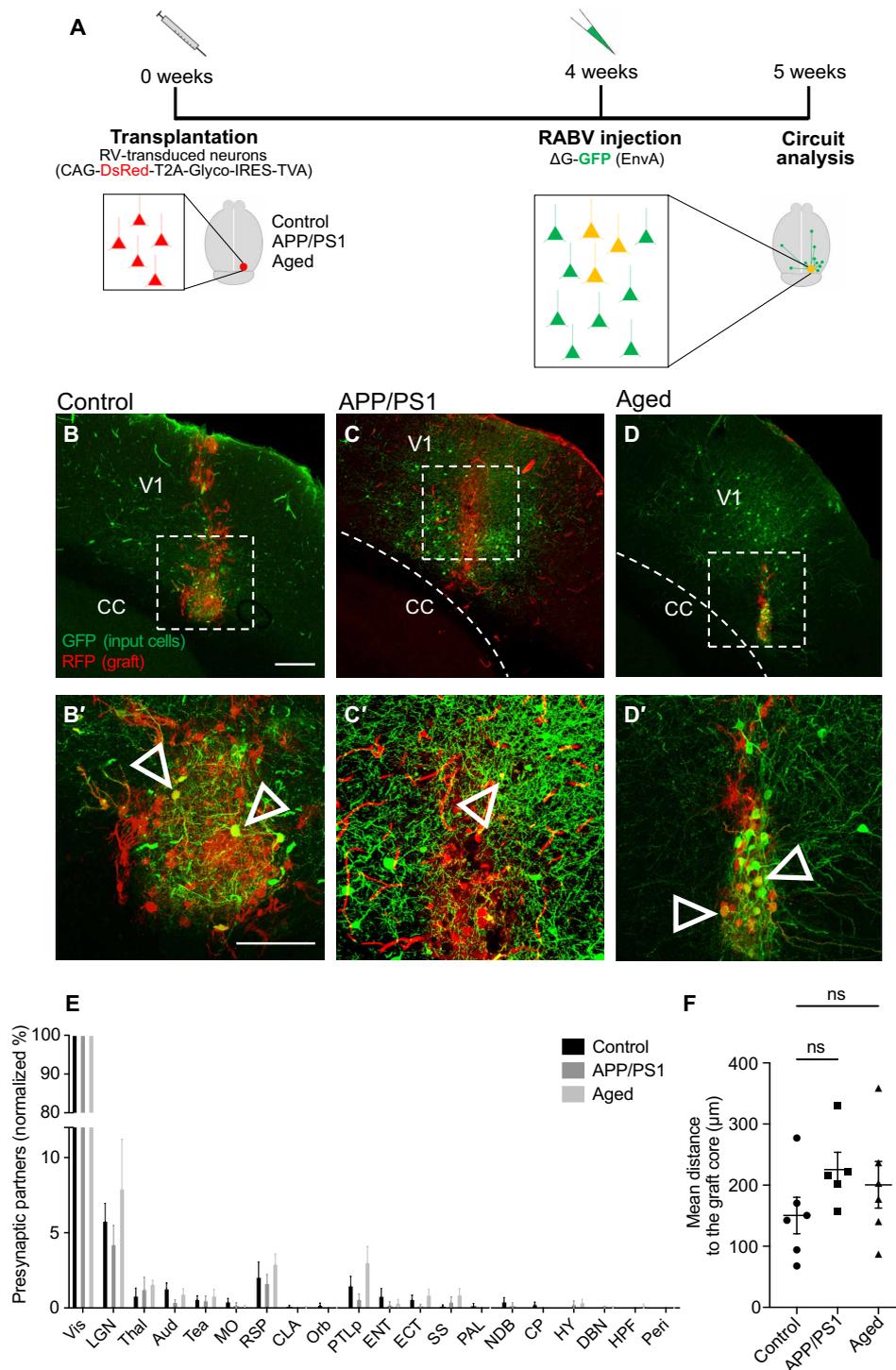
Fig. 1. Transplanted neurons integrate into the cortex of APP/PS1 and aging mice. (**A**) Scheme of the experimental procedure. (**B** to **D**) Representative micrographs of the transplantation sites in WT control (B) ($n = 6$), amyloid plaque–loaded transgenic (APP/PS1) (C) ($n = 5$), and WT aged (D) ($n = 6$) cortices at 5 wpt (sagittal sections, confocal z-projection). CC, corpus callosum. Scale bar, 200 μm. TVA expression in donor cells renders them susceptible to RABV (EnvA) infection, resulting in RFP+/GFP+ coexpressing starter neurons [insets shown in high magnification in (B') to (D'); white arrowheads]. Scale bar, 100 μm. Expression of the G protein (A) in transplanted cells allows the RABV to propagate retrogradely across one synapse, resulting in GFP (or RFP, depending on fluorescence of RABV)–only labeling of first-order presynaptic neurons. Micrographs B (B') and D (D') show grafts consisting of E14 cultured and virally labeled donor cells (RFP+). Micrograph C (C') shows a graft consisting of E18 donor cells (GFP+). In this micrograph, for the purpose of consistency, the donor cell was pseudo-colored to red, and the presynaptic cells to green. (**B'** to **D'**) Examples of starter neurons (RFP+/GFP+; arrowheads) that can be found within the graft in all three conditions. (**E**) Distribution of presynaptic partners across the different input areas of the ipsilateral hemisphere. The data are presented as percentages normalized by the region with the highest number of traced cells in each group (Vis); see Fig. 2 for abbreviations of anatomical areas. (**F**) Mean distance of presynaptic partners within the Vis to the graft core (per animal) measured in micrometers. Data are means ± SEM. Kruskal-Wallis test followed by Dunn's post hoc test; ns, not significant.
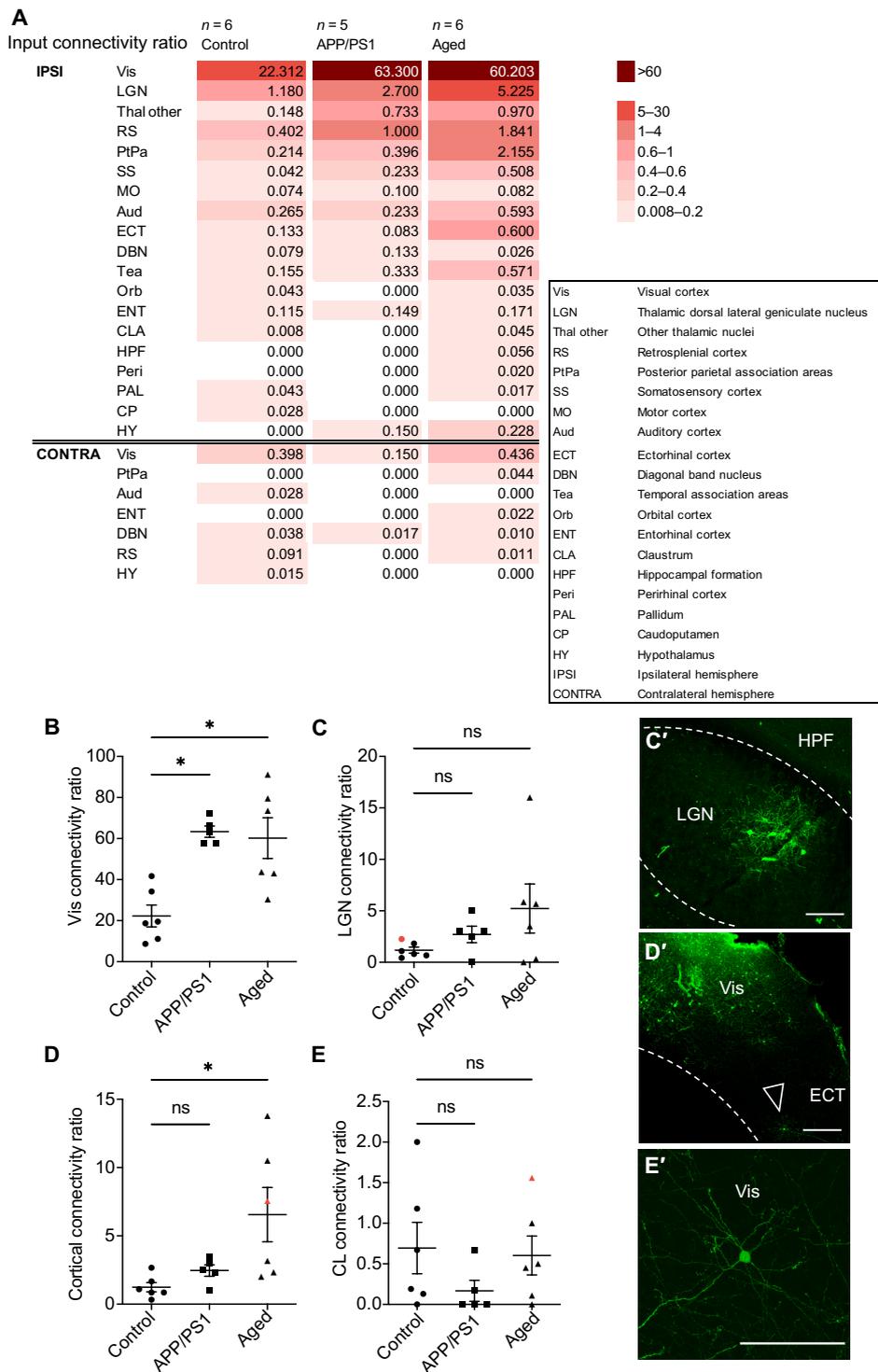
A
Input connectivity ratio

		n = 6 Control	n = 5 APP/PS1	n = 6 Aged
IPSI	Vis	22.312	63.300	60.203
	LGN	1.180	2.700	5.225
	Thal other	0.148	0.733	0.970
	RS	0.402	1.000	1.841
	PtPa	0.214	0.396	2.155
	SS	0.042	0.233	0.508
	MO	0.074	0.100	0.082
	Aud	0.265	0.233	0.593
	ECT	0.133	0.083	0.600
	DBN	0.079	0.133	0.026
	Tea	0.155	0.333	0.571
	Orb	0.043	0.000	0.035
	ENT	0.115	0.149	0.171
	CLA	0.008	0.000	0.045
	HPF	0.000	0.000	0.056
	Peri	0.000	0.000	0.020
	PAL	0.043	0.000	0.017
	CP	0.028	0.000	0.000
	HY	0.000	0.150	0.228
CONTRA	Vis	0.398	0.150	0.436
	PtPa	0.000	0.000	0.044
	Aud	0.028	0.000	0.000
	ENT	0.000	0.000	0.022
	DBN	0.038	0.017	0.010
	RS	0.091	0.000	0.011
	HY	0.015	0.000	0.000

Color scale:
- >60
- 5–30
- 1–4
- 0.6–1
- 0.4–0.6
- 0.2–0.4
- 0.008–0.2

Abbreviation	Description
Vis	Visual cortex
LGN	Thalamic dorsal lateral geniculate nucleus
Thal other	Other thalamic nuclei
RS	Retrosplenial cortex
PtPa	Posterior parietal association areas
SS	Somatosensory cortex
MO	Motor cortex
Aud	Auditory cortex
ECT	Ectorhinal cortex
DBN	Diagonal band nucleus
Tea	Temporal association areas
Orb	Orbital cortex
ENT	Entorhinal cortex
CLA	Claustrum
HPF	Hippocampal formation
Peri	Perirhinal cortex
PAL	Pallidum
CP	Caudoputamen
HY	Hypothalamus
IPSI	Ipsilateral hemisphere
CONTRA	Contralateral hemisphere

Fig. 2. Excessive input connectivity to transplants in APP/PS1 and aging cortices. (**A**) Color-coded average CR for all brain-wide input areas in WT control ($n = 6$), transgenic APP/PS1 ($n = 5$), and WT aging ($n = 6$) mice at 5 wpt (the darker the color code, the higher the CR). For calculation of the CR, the number of input neurons in a given area was normalized to the number of starter cells in the transplant. The average CRs per condition were calculated with each animal as one data point. Right: List of abbreviations. (**B** to **E**) CRs of the different regions indicated on the y axis and the different brain environments indicated on the x axis. In (D), cortical regions considered were RS, PtPa, SS, MO, Aud, ECT, ENT, Tea, and Orb. (**C′**) Example image of presynaptic partners (source animal is highlighted in red on the respective graph) found in the LGN. HPF, hippocampal formation. Scale bar, 100 μm. (**D′**) Example image of a presynaptic partner found in a cortical region different than V1, in this case, the ECT (arrow-head). Scale bar, 200 μm. (**E′**) Example image of a presynaptic partner found in the contralateral hemisphere (in V1). Scale bar, 100 μm. Data are means ± SEM. Kruskal-Wallis test followed by Dunn's post hoc test; *$P \leq 0.05$.

described before (18). The number of input neurons in a given brain region was divided by the total number of starter neurons (RFP$^+$/GFP$^+$) within the graft to calculate the CR and to allow comparison between mice and conditions. The number of starter neurons varied between transplants but did not differ systematically between the experimental conditions (fig. S2, F and G). A total of 26 innervating brain regions were mapped (Fig. 2A), all known to innervate V1 (51, 52), indicating the absence of aberrant connectivity in all these conditions. We consider this an important finding for cell-based therapy for AD patients and elderly.

Most inputs derived from local visual cortex (Vis) neurons, with the highest CR consistently found for this region (Fig. 2A), as is the case for V1 neurons in the naïve mouse brain (18, 51, 52). The CR for this anatomical region (Vis-to-graft, intra-area) in the control group was very similar to that previously measured for endogenous connections within this area using the same tracing technology and analytical pipeline. In contrast, this local innervation was significantly elevated in APP/PS1 transgenic mice (Fig. 2, A and B), as indicated by a threefold increase in CR. This was not the case for other regions and the main afferent of V1, the thalamic dorsal lateral geniculate nucleus (LGN) (51), with no significant difference in the LGN-to-Vis connectivity in APP/PS1 as compared to WT control brains (Fig. 2, A and C). Notably, the CR for other cortical regions with high plaque deposition, such as RS, PtPa, SS, MO, Aud, ECT, ENT, Tea, and Orb (see abbreviations in Fig. 2A), was comparable between APP/PS1 and control WT brains of equal age and from the same colony and background (Fig. 2D). This was also the case for the contralateral hemisphere (Fig. 2E; for the exact numbers of traced neurons per mouse and brain area, see data S2). Thus, in the amyloid plaque–loaded cortex, the local inputs to the graft are specifically enhanced. This is not related to the plaque load in the innervating region, as relatively normal connectivity from other cortical regions with similar plaque load was observed. Notably, however, statistical significance of CR changes in regions with low CR and hence traced neurons present only in some animals may be missed.

Excessive cortical connectivity of neuronal grafts in the cortex of aging mice

To determine whether the above findings were specific to the APP/PS1 condition, we examined the synaptic integration of the same donor cells in the cerebral cortex of 16- to 18-month-old WT mice. Intravisual host-graft connectivity was significantly increased in the aging cortex compared to 8-month-old WT control mice (Fig. 2, A and B). The visual cortex CR was similar to the one observed in transgenic APP/PS1 mice, although with greater interindividual variability. In addition, we noted a significant increase in CR also from other cortical regions only in the aged brains (Fig. 2D). In addition, the mean CR of LGN inputs was fivefold higher compared to controls but failed to reach statistical significance because of a large interindividual variation (Fig. 2C). Conversely, interhemispheric connectivity was well comparable to the control and other experimental groups (Fig. 2E; for the exact numbers of traced neurons per mouse and brain area, see data S2). Together, in both host environments, transplanted neurons receive excessive inputs from the local or overall cortical circuitry. Unexpectedly, the aging cortex, which is the model with milder gliosis (fig. S1), exhibited a more widespread effect in graft connectivity as compared to the 8-month-old APP/PS1 transgenic mice, although the higher variability across individuals among the aged mice prompts careful consideration of these results.

Comprehensive proteome analysis of cortical environments inducing host-graft hyperconnectivity

Given the connectivity differences in the two conditions that also differ in the extent of gliosis, we used unbiased proteomics to understand the composition of these environments causing graft hyperconnectivity. Tissue punches were collected from the visual cortices of both brain hemispheres of five transgenic 8-month-old APP/PS1 and nine C57BL/6J mice (four aging WT and five WT 8-month-old controls), i.e., at the time and exact age when transplantation would be performed. State-of-the-art liquid chromatography–tandem mass spectrometry (LC-MS/MS) allowed reproducible detection of 5368 proteins. About 7.2%, i.e., 384 proteins, were significantly enriched in transgenic APP/PS1 tissue samples relative to the WT age-matched control samples (Fig. 3A; see table S1A for detailed P values). As expected, amyloid-β A4 protein (APP) was significantly more abundant in the cortex of APP/PS1 transgenic mice (Fig. 3A), consistent with its overexpression under the Thy1 promoter in these mice (32). Further validating the amyloidogenic model, β-secretase 1 (Bace1), a protein known to initiate the APP processing and to accumulate around plaques (53), was also significantly increased (table S1A), as could be confirmed by immunostaining specifically surrounding the plaque regions (fig. S4). In line with the prominent reactive astrogliosis upon amyloid deposition in these mice (47, 48, 54, 55), vimentin (Vim) and GFAP were significantly increased (Fig. 3A). Along with reactive gliosis, we detected differentially regulated components of the extracellular matrix (ECM), such as vitronectin (Vtn) and several integrins like integrin β2 (Itgb2). Members of the classical complement system, complement C4-B (C4b) and complement subcomponent C1q, subunits a, b, and c (C1qa, C1qb, and C1qc), were significantly enriched in the APP/PS1 group (Fig. 3A), as also confirmed by immunostaining (Fig. 3, F, G, and I). Gene Ontology (GO) term analysis corroborated these findings, showing a significant enrichment of "complement activation, classical pathway" along with "synapse pruning," including immunoglobulin κ constant (Igkc), immunoglobulin heavy constant γ 2b (Ighg2b), and integrin α (Itgam), besides C1qc, C1qb, and C1qa (Fig. 3B and table S1B). The most significant GO terms were all related to the immune system and inflammatory processes, such as "immune response" including C1qa, C1qb, C1qc, clusterin (Clu), APP, signal transducer and activator of transcription 1 (Stat1), or the immune-related guanosine triphosphatase family M protein 1 (Irgm1), among others. Thus, inflammation and immune response may contribute to activate microglia-mediated synapse removal via the complement system (56, 57). Consistent with the synaptic dysfunction and loss during amyloidosis, proteins related to neuronal activity and synapse function, such as leucine-rich repeat and fibronectin type 3 domain–containing protein 2 (Lrnf2) and glutamate ionotropic receptor kainate type subunit 5 (Grik5), were significantly down-regulated in the APP/PS1 samples (Fig. 3A and table S1B). Among the significant GO terms of down-regulated proteins was "positive regulation of RNA-splicing," which may contribute to neuronal dysfunction given the profound importance of splicing for neuronal function.

When comparing the cortex samples from 17-month-old aged WT to those of 8-month-old WT control mice, 175 proteins differed significantly in their abundance (Fig. 3C; see table S1C for detailed P values), thus only about half of the total number of significantly
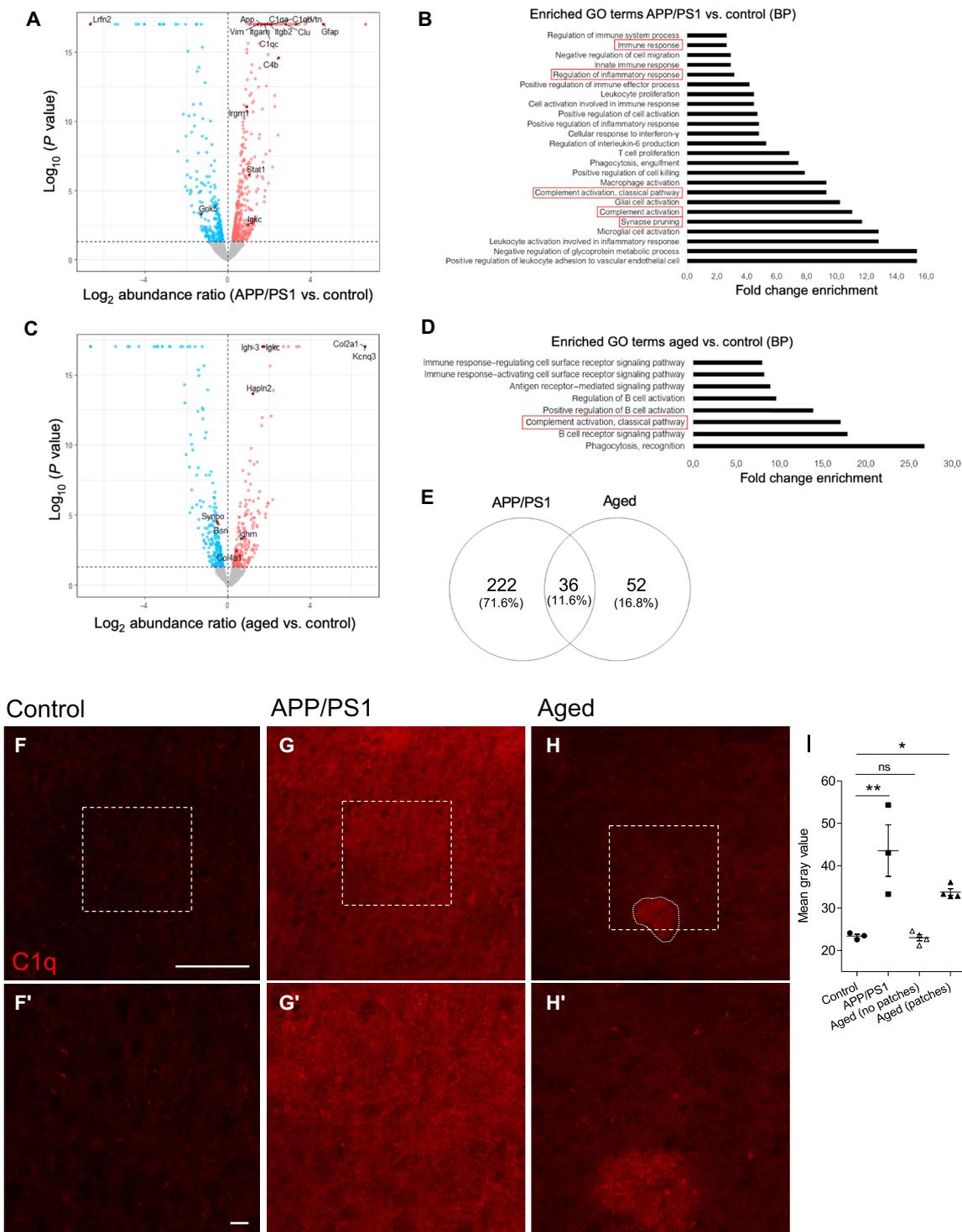
Fig. 3. Comprehensive proteome changes in APP/PS1 and aging cortices compared to controls. (**A** and **C**) Volcano plots showing mean protein abundance ratios comparing transgenic APP/PS1 (A) ($n = 10$ hemispheres from five mice) or WT aging (C) ($n = 8$ hemispheres from four mice) cortex with WT controls ($n = 10$ hemispheres from five mice). Significantly different proteins ($-\log_{10} P$ value, y axis; $\log_2$ abundance ratio, x axis) are indicated in color (enriched in red and reduced in blue). (**B** and **D**) Most relevant enriched GO terms [BP (biological process)] in transgenic APP/PS1 and WT aging brains versus WT controls. (**E**) Venn diagram showing the overlap of proteins enriched in APP/PS1 and aging cortex versus control. (**F** to **H**) Micrographs of C1q immunostaining in the visual cortex of animals from the three experimental conditions indicated on the top. (**F'** to **H'**) Corresponding higher-magnification insets of (F) to (H). The dashed line (H) shows a C1q-high patch in the aging cortex, and (**I**) shows the mean gray value quantification comparing the different conditions (sagittal sections, confocal z-projection; scale bars, 100 μm and 10 μm). Data are means ± SEM. One-way analysis of variance (ANOVA) followed by Holm-Sidak correction; *$P \leq 0.05$ and **$P \leq 0.005$ ($n = 3$ to 4). Proteome statistical analysis was done as described by Navarro *et al.* (*79*); $P \leq 0.05$.

regulated proteins in the APP/PS1 cortex. Several members of the ECM were also significantly increased in the aged cortex, but differed from those in the APP/PS1 cortex, e.g., hyaluronan and proteoglycan link protein 2 (Hapln2), laminins, and collagen. Bace1 was also significantly increased in this condition, as confirmed also by immunostainings (fig. S4). Among the significantly enriched GO terms for down-regulated proteins was "negative regulation of proteolysis" with several peptidase inhibitors. Among the enriched proteins, also in the aged cortex, the GO term "complement activation, classical pathway" was significantly enriched including proteins such as Igkc, Ighg2b (Fig. 3, C and D, and table S1D), and several others, such as Ig μ chain c region (Ighm) involved in the immune response (58). Other significant GO terms were related to the immune system, again including proteins such as Igkc, Ighg2b, and Ighm (Fig. 3D). Moreover, synapse proteins like bassoon (BSN) or synaptopodin (Synpo) were found down-regulated (Fig. 3C). Together, immune regulation, complement activation, and synapse loss are common hallmarks of both the aging and the amyloid-loaded cortex.

To identify factors relevant for excessive transplant connectivity, we examined the proteins regulated in both connectivity-promoting environments, such as Bace1 (Fig. 3E and fig. S4). We noted that the term "phagocytosis, recognition" was commonly enriched, which consisted of the complement system–related proteins Igkc and Ighg2b, as well as Ig γ-2B chain C region (Igh-3) and collagen α-1(II) chain (Col2a1; table S1, E and F). Many of the commonly regulated proteins are related to synaptic function and the complement system, such as C1q, and are involved in early synapse loss in AD mouse models (56) and in the aging brain (59, 60). Immunostaining confirmed the increased levels of C1q in both the plaque-loaded and aged cerebral cortex (Fig. 3, F to H) with a patchy appearance in the latter, which was reported before (59). In the APP/PS1 cortex, C1q was markedly and homogeneously increased (Fig. 3, G and I), which also explains why it is significantly enriched in the proteome of the APP/PS1 cortex, but not the aged cortex, where it appears only in patches (Fig. 3, H and I). The patchy C1q and accordingly synapse loss may well relate to the higher variability of host-graft connectivity in the aged host brains. Together, this analysis implies the up-regulation of the C1q protein and a related loss of synapses as a possible cause for the increased availability of afferents in the recipient parenchyma, ready to connect with fully competent transplanted young neurons rather than diseased and aged endogenous counterparts.

DISCUSSION

Here, we investigated the integration of transplanted fetal neurons into brain circuits affected by amyloidosis or altered in the course of aging. This revealed an excessive innervation from local neurons in both conditions, and additionally from other cortical regions in aged mice. This is a notably different outcome compared to controls or young mice subjected to a cortical injury with mild inflammatory reaction, where new connectivity is quantitatively similar to the naïve connectivity (18).

Technical considerations

Before evaluating the new insights based on RABV tracing, it is important to consider technical aspects. For instance, the G protein expression may be influenced by amyloidosis or inflammation. To probe for this, we applied β amyloid (Aβ$_{1-42}$) fibrils and inflammatory stimuli,

such as lipopolysaccharides (LPS), interferon-γ, or interleukin-1β, to the cells we would normally transplant after infecting them with the G protein–expressing virus (fig. S5). Immunostaining for the G protein and quantification of the signal revealed similar G protein levels despite these marked stimuli in vitro (fig. S5H). Thus, inflammation or amyloid does not regulate G protein levels expressed under the robust chicken β-actin promoter (CAG).

In addition, neuronal activity may differ across our experimental groups and hypothetically change RABV propagation if silent and active synapses are differentially conducive. The amyloid-loaded brains have an increased number of silent and hyperactive neurons, with the latter located in the vicinity of the plaques (61, 62). Increased numbers of hyperactive neurons occur at early stages, while the balance between hyperactive and silent neurons is achieved in the 8-month-old APP/PS1 transgenic mice used here. While altered levels of neuronal activity may be highly relevant for synaptic competition between transplanted and endogenous neurons (see below), these do not regulate G protein levels as shown previously (63). Neither blocking action potentials nor promoting synaptic transmission has an effect on G protein levels or monosynaptic RABV tracing (63). Hence, we conclude that G protein levels are unlikely to be altered and majorly influence the input tracing in the conditions examined here.

Basic principles of transplanted neuron integration

Our work elucidates several basic principles underlying the integration of new neurons into brain circuits demonstrating foremost that neuron loss is not a prerequisite. There is no neuron loss in the cerebral cortex of APP/PS1 transgenic mice at 8 months of age (47) and in aging WT mice (64, 65), yet new neurons receive even more connections than in models with previous neuron loss (18). This effect is restricted to local connectivity in APP/PS1 mice and, hence, not directly related to the amyloid plaque load that is present throughout the cerebral cortex. Notably, however, the plaque load was suggested to be highest in more posterior regions such as the hippocampus and the visual cortex (66) and may thus correlate to the higher local inputs observed here in the visual cortex. In the aging brain, supranumerary inputs also derive from other cortical regions, implying that the cause for hyperconnectivity is slightly more pronounced and widespread in this environment and hence, at least in this condition, unrelated to plaque load. However, the degree of reactive gliosis, as monitored by reactive astrogliosis and microglia activation and expansion, is also not a major predictor and determinant of the input connectome. This was equally excessive in the mild gliosis condition of the cortex undergoing normal aging and the amyloid-loaded cortex with much higher levels of astrocyte and microglia number/activation.

As these conditions and the ensuing gliosis differ at the molecular level, we explored which factors may render these brain environments so conducive for excessive inputs onto grafted neurons by unbiased proteome analysis. Activation of the complement pathway and immune system were the most pronounced common hallmarks in both environments and may be key for the observed hyperconnectivity. Complement activation has a well-documented role in tagging synapses for elimination by microglia (56, 67, 68), a process that may be enhanced in these immune-activated environments (56, 69). Knocking out C1q in APP/PS1 transgenic mice leads to a decrease in neuropathology, especially less activated glia cells, suggesting that C1q also contributes to gliosis (70). Synapse loss is mediated by complement up-regulation (56), and increased C1q protein is associated

with postsynaptic sites in the prefrontal cortex of macaque in the course of aging (*71*). We therefore propose that synapse loss mediated by inflammation and complement activation rather than loss of neurons fosters the excessive input connectome to grafted neurons in aging and amyloid-loaded brains.

Neuronal activity plays a key role in synaptogenesis and synaptic plasticity, and has been described as a crucial mechanism during synaptic competition for integration of adult-generated neurons in the dentate gyrus (*72–75*). After transplantation, like in adult neurogenesis, new neurons that are particularly active and excitable compete with preexisting neurons and synapses. Thus, synapses formed onto the transplanted neurons may be preferred because of higher postsynaptic activity compared to synapses on preexisting neurons. Consequently, activity-dependent mechanisms favoring the transplanted neurons over neurons preexisting in the pathological environment may contribute to the hyperinnervation of neurons transplanted into the amyloidosis and aged environments. Again, the similar levels of hyperconnectivity observed between the transplants into amyloid-loaded brains and the normal aged brain argue against a major role of an imbalance between synaptic excitation and inhibition in the APP/PS1 mice (*61*). Likewise, we could not detect any differences in the number of interneurons stained for parvalbumin in V1 of the host environments (fig. S6), thus ruling out their selective death as a major contributor to altering excitation/inhibition balance in this context.

Clinical relevance and conclusion
Beyond the mechanisms mediating neuron integration, our work highlights a further need to optimize conditions for adequate graft connectivity in AD and elderly patients. Conditions involving synaptopathy need to be carefully considered and possibly alleviated before implementing neuronal replacement strategies in human patients. This work shows that it is not possible to extrapolate from transplantation studies in stroke or TBI the outcome of transplantation in aged or amyloid-loaded brains (*75*), as is likewise the case for profound differences in the type of reactive gliosis between these conditions (*33*). Last, it is of equal importance to monitor the connectome to endogenous neurons in the above conditions in preclinical models and aim at elucidating it by modern imaging technologies in patients' brains.

MATERIALS AND METHODS
Experimental design
Animals
Animals were kept in the animal facility of the Biomedical Centre, LMU Munich, and experiments were performed in compliance with German and European Union guidelines and approved by the Government of Upper Bavaria. Mice were kept in specific pathogen–free conditions and had housing conditions of 12-hour:12-hour light-dark cycle, food, and water ad libitum. APP/PS1 transgenic mice express human APP ($APP_{KM670/671NL}$) and mutated PS1 ($PS1_{L66P}$) under Thy1 promoter and were bred on a C57BL/6J background (*32*). APP/PS1 transgenic mice (*32*), APP/PS1 WT littermates, and C57BL/6J mice (both used as controls) underwent surgery at 8 months of age. C57BL/6J mice at 16 to 18 months of age were part of the same colony and used for the aging condition. Both female and male mice were used for all conditions (see fig. S2G for the ratio of male and female mice).

Embryonic cortex collection, cell culture, and viral labeling
Neocortical tissue from E14 C57BL/6J embryos was dissociated using Hanks' balanced salt solution (HBSS) buffered with Hepes (10 mM; Life Technologies). A density of 200,000 cells per well was plated into a poly-D-lysine (Sigma-Aldrich)–coated 24-well plate using medium consisting of high-glucose Dulbecco's modified Eagle's medium (DMEM) GlutaMAX (4.5 g/liter), penicillin-streptomycin (Life Technologies), and 10% fetal bovine serum (FBS; PAN-Biotech). The cells were transduced 2 to 4 hours later with 1.0 to 1.2 µl of Moloney murine leukemia virus–derived retrovirus (CAG-DsRedExpress2-2A-Glyco-IRES2-TVA; multiplicity of infection: 2.0×10^6 to 3.0×10^6) per well to provide the FP DsRed, the G protein, and TVA receptor to the donor cells, which is needed for tracing of the input connections later on. Note that the absence of infective viral particles in the culture supernatant at 2 to 4 days in vitro was ensured by adding the culture supernatant to uninfected cultures and monitoring the absence of any FP signal. For G protein control transplantations, cells were transduced with a retrovirus providing only the TVA receptor and DsRed to the donor cells (CAG-DsRedExpress2-IRES2-TVA; multiplicity of infection: 2.0×10^6 to 3.0×10^6) to ensure that transsynaptic spread only occurs when G protein is expressed. In the following 2 days, the medium was gradually replaced with neuronal differentiation medium consisting of high-glucose DMEM GlutaMAX (4.5 g/liter), penicillin-streptomycin, and B27 (1:50; Life Technologies). Cells were cultured 3 to 5 days before transplantation. On the day of transplantation, cells were washed three times with 1× phosphate-buffered saline (PBS) to remove all viral particles, then dissociated and trypsinized (0.025% of trypsin-EDTA), and collected into a tube filled with FBS-containing medium (1:1) to inhibit the enzymatic reaction. After centrifugation, the remaining cell pellet was resuspended in neuronal differentiation medium, cells were counted, and a final cell suspension of 50,000 cells/µl was prepared for subsequent transplantation (cells were kept on ice until surgery).

Quantification of glycoprotein levels
E14 cortical neurons were dissociated and cultured for 5 days as described above. On day 5 (time point when cells would be used for transplantation), the medium was changed and substituted with differentiation medium containing one of the following stimuli (*n* = 3): 2.5 mM amyloid-β fibrils ($Aβ_{1–42}$) in dimethyl sulfoxide (DMSO), LPS (100 ng/ml) in H_2O, interleukin-1β (50 ng/ml) in 0.1% bovine serum albumin (BSA), and interferon-γ (20 ng/ml) in 0.1% BSA, together with their respective vehicle controls. Twenty-four hours after stimulation, the cells were washed with PBS and fixed with 4% paraformaldehyde (PFA) in PBS for 15 min at 4°C. To prepare amyloid fibrils, the day before the incubation, 0.1 mg of lyophilized $Aβ_{1–42}$ was vigorously dissolved in 4 µl of anhydrous DMSO. Two hundred microliters of DMEM was added, and the mix was sonicated for 20 min in a water bath. The sonicated mix was then incubated overnight at 37°C with agitation and protected from light.

For the quantification of G protein staining, 40× z stacks (*n* = 3 coverslips per condition) were imaged (Zeiss, LSM 710). A maximum intensity projection was generated, and on the RFP channel, the area around the soma of 10 RFP⁺/Dapi⁺ cells was outlined as well as the nuclei of 10 RFP⁻/Dapi⁺ cells for normalization. The mean gray value of G protein staining in the far-red channel was measured in the outlined cells, and the mean gray values were normalized by subtracting the average mean gray value of the RFP⁻/Dapi⁺ cells (i.e., background) of each coverslip.

Surgeries

For all surgical procedures, the animals received intraperitoneally injected anesthesia and postoperative treatment as approved by the Government of Upper Bavaria. The anesthesia consisted of fentanyl (0.05 mg/kg; Janssen), midazolam (5 mg/kg; Roche), and medetomidine (0.5 mg/kg; Fort Dodge) and was antagonized by subcutaneous administration of atipamezole (2.5 mg/kg, Janssen), flumazenil (0.5 mg/kg; Hexal), and buprenorphine (0.1 mg/kg; Essex) at the end of each surgery.

Transplantation

C57BL/6J mice (8-month-old WT controls and 16- to 18-month-old WT mice for the aging condition), APP/PS1 WT littermates (also used as controls), and APP/PS1 transgenic mice were transplanted with 1 μl of cell suspension (~50,000 cells) into the visual cortex of the right hemisphere using the following coordinates from lambda: 2.5 ± 0.3 mm mediolateral and 0.0 ± 0.2 mm anteroposterior. First, a cranial window was drilled to open the skull. Subsequently, donor cells were transplanted using a Hamilton syringe gauge 33 at a cortical depth from 0.6 to 0.2 mm at lowest (manual) possible speed. The bone lid was carefully placed back onto the brain surface, and the skin was sutured.

For some transplantations (fig. S2), neocortical tissue from triple-transgenic E18 Emx1Cre/G-TVA/GFP embryos (76–78) was dissociated without culturing or viral labeling (fig. S2G for experiments with acutely dissociated versus cultured cells). For this purpose, only GFP fluorescent brains were picked for dissociation, as these embryos express the G protein and TVA receptor needed for later RABV tracing. Cell dissociation from the cortices was performed as described above for cultured cells. The embryonic cells were resuspended in neuronal differentiation medium and centrifuged. The cell pellet was resuspended in the same medium, cells were counted, and a cell suspension was prepared in the same way as described for cultured embryonic cells.

Rabies virus injection for transsynaptic tracing

To analyze brain-wide synaptic inputs to the grafted cells, we injected a genetically modified RABV (EnvA-coated and ΔG-eGFP or ΔG-mCherry) (50) 4 weeks after transplantation, as described before (18). During the surgical procedure, RABV was injected around the graft area within the visual cortex. To do so, the previously drilled cranial piece was reopened and the RABV was injected using a thin glass capillary inserted into an automated nanoinjector (Nanoliter; World Precision Instruments). Three injections around the graft area were performed (200 nl per injection; injection speed of 1 nl/s) to ensure an even distribution of RABV at the graft site. In addition, for the purpose of controlling the leakiness of the modified RABV, a craniotomy was drilled above the visual cortex of WT mice and the RABV was injected (in the same way as in transplantation experiments).

Immunostainings

One week after RABV injection, mice were transcardially perfused under ketamine (100 mg/kg) + xylazine (10 mg/kg) anesthesia. For perfusion procedure, 1× PBS was supplied for ~5 min followed by 4% PFA for ~20 min. Afterward, the brains were carefully dissected and subsequently stored in 4% PFA at 4°C overnight. For connectome analysis, the brains were cut serially into 70-μm sagittal slices using a vibratome. Free-floating sections were washed and incubated in blocking solution (3% BSA and 0.5% Triton X-100 in 1× PBS) for 2 hours, and the following antibodies were diluted in blocking solution: chicken anti-GFP (1:1000; Aves Labs) and rabbit anti-RFP

(1:1000; Rockland Immunochemicals). Sections were incubated for 48 hours at 4°C, washed, and incubated with the following secondary antibodies for 3 hours at room temperature (RT): anti-chicken Alexa Fluor 488 (1:1000; Invitrogen) and anti-rabbit Cy3 (1:1000; Dianova). Before mounting, 4′,6-diamidino-2-phenylindole (DAPI; 1:1000; Sigma-Aldrich) was applied to the sections for 15 min to label cell nuclei.

For C1q, GFAP, Iba1, and parvalbumin immunostainings, the same staining procedure applies except that 50-μm sections were used to ensure better penetration of the antibody. Rabbit anti-C1q (1:1000; Abcam), mouse anti-GFAP (1:500; Sigma-Aldrich), rabbit anti-Iba1 (1:1000; Synaptic Systems), or mouse IgG1 anti-parvalbumin (1:250; Sigma-Aldrich) antibodies were applied one or two overnights at 4°C, and secondary anti-rabbit or anti-mouse Alexa Fluor 647 or anti-rabbit or anti-mouse Alexa Fluor 488 was applied for 3 hours at RT followed by DAPI staining.

For Bace1 immunostaining, the tyramide signal amplification (TSA) biotin kit (Akoya Biosciences) was used. Briefly, free-floating 50-μm sections were blocked in 2% BSA and 0.5% Triton X-100 in PBS for 1 hour at RT. Rabbit anti-Bace1 (1:250; Cell Signaling Technology) antibody was incubated in blocking solution for two overnights at 4°C. After 1× PBS washes, biotinylated anti-rabbit secondary antibody (1:500; Akoya Biosciences), anti-mouse Alexa Fluor 488 antibody (1:500; Thermo Fisher Scientific), and DAPI (1:1000; Sigma-Aldrich) were incubated in blocking solution overnight at 4°C. After PBS washes, endogenous peroxidase activity was quenched by incubating the sections in 0.3% H_2O_2 for 60 min at RT. Sections were subsequently washed in PBS and incubated with streptavidin–horseradish peroxidase reagent (1:100; Akoya Biosciences) in PBS for 1 hour at RT. Sections were washed again in PBS and treated with tyramide signal amplification tetramethylrhodamine reagent (TSA TMR, TS-000101 Akoya Biosciences) diluted 1:75 in amplification siluent (FP1050, Akoya Biosciences) for 8 min at RT. The sections were washed in PBS and mounted with Aqua-Poly/Mount (Polysciences).

For the immunocytochemical analysis of G protein, cells were fixed by PFA as described above, followed by washes in PBS and incubation for 1 hour at RT with 5% BSA and 0.1% saponin in PBS. Primary antibodies were incubated overnight at 4°C in antibody dilution buffer (1% BSA and 0.1% saponin in PBS). The following primary antibodies were used: mouse IgG2a anti-glycoprotein IC5 (1:150; Bio-Rad), rabbit anti-RFP (1:500; Rockland Immunochemicals), and mouse IgG1 anti-GFAP (1:500; Sigma-Aldrich). Following primary antibody incubation, coverslips were washed three times with PBS and incubated for 3 hours at RT with secondary antibodies in antibody dilution buffer (anti-mouse IgG2a Alexa Fluor 647, anti-rabbit Alexa Fluor 546, and anti-mouse IgG1 Alexa Fluor 488). Coverslips were washed, stained with DAPI (1:1000; Sigma-Aldrich), and mounted with Aqua-Poly/Mount (Polysciences).

Quantification of input connections

Each brain section (in serial order) was checked for FP-labeled input cells, and whenever cells were detected, a 10× tile scan of the whole section was made with automated scanning, tile alignment, and image stitching using an epifluorescence microscope (Zeiss, Axio Imager M2). The resulting image from the multitile scan was overlapped with the corresponding section of the Allen Brain Reference Atlas of the adult mouse brain. The most lateral brain sections are not available in this Reference atlas, and thus, for these sections, the tiled image was aligned with sections retrieved from Brain

Explorer 2 (Allen Institute for Brain Science) to identify the correct anatomical region where the cells locate. Whenever a high number or closely assembled labeled cells were found, z stack scanning was performed with a laser scanning confocal microscope (Zeiss, LSM 710) using a 40× objective. In sections that contained the graft area, all FP⁺ input cells with neuronal morphology and all GFP⁺/RFP⁺ cells with neuronal morphology (starter cells) were counted. The CR for a given brain region was calculated by dividing the number of total FP⁺ input cells in that region by the total number of GFP⁺/RFP⁺ starter neurons within the graft in V1. Data are presented as means ± SEM calculated between different mice for each condition ($n \geq 5$).

Image analysis

An epifluorescence microscope with a motorized stage and 10× objective (Zeiss, Axio Imager M2) and a laser scanning confocal microscope (Zeiss, LSM 710) with a 40× objective were used for imaging. To analyze whole-brain input connections, the ZEN 2012 (Zeiss) and ImageJ 1.48p software were used. With the plugin "Cell counter" in ImageJ and by carefully checking serial sections of the confocal z stacks, exact numbers of starter and input cells were counted. To estimate the graft volume, the area covered by the fluorescent transplanted cells was manually outlined and quantified (ImageJ) on all the histological sections spanned by the grafts. The volume was then calculated by the sum of all the areas multiplied by the thickness of the sections (70 μm). To calculate the distance of the presynaptic partners to the graft in V1, a straight dorsoventral line was drawn from the cortical surface along the transplant core and the (X, Y) position of each presynaptic partner's soma relative to this line was measured (ImageJ). These coordinates were used to calculate the distance between each cell to the graft midline.

For the microglia morphology analysis, two images per mouse of four mice per condition were analyzed. The images were obtained using a 40× water objective (numerical aperture of 1.1) on a Zeiss confocal microscope (LSM 710). The size of each image was 1024 pixels by 1024 pixels with a 0.7-μm z-step. Analysis was performed in 3D with Imaris software (9.6.0; Bitplane) using filament tracing and surface tools. The algorithm chosen for the filament tracing was Autopath with no loops, and the detection of starting points was set to 10.4 μm to target the cell soma. For the surface function, the thresholding was based on absolute intensity, and the split touching objects function was enabled with a seed point diameter of 10 μm. The detected cells were then classified on the basis of their volume.

For C1q and Bace1 quantifications, images were acquired using a Zeiss confocal microscope (LSM 710) with a field of view of 212 μm by 212 μm and 1-μm z-step as well as 566 μm by 566 μm and 2-μm z-step, respectively. The mean gray value was measured on z-projections and from two to three sections of three to four animals per condition (ImageJ). To measure the mean gray value of Bace1 staining in APP/PS1 sections, three plaques per section were manually delineated and three areas of 100 μm by 100 μm free of plaques were quantified. Similarly, for C1q measurements in the aged group, C1q signal patches were manually delineated and 50 μm–by–50 μm areas without patches were quantified. For quantifications of parvalbumin⁺ cells, confocal images were taken with a field of view of 566 μm by 566 μm and 2-μm z-steps. We quantified positive cell somas containing DAPI⁺ nuclei in a 500 μm–by–500 μm area per image.

Mass spectrometry

Eight-month-old WT control C57BL/6J (n = 5 mice), 17-month-old aged C57BL/6J (n = 4 mice), and 8-month-old APP/PS1 transgenic mice (n = 5 mice) were sacrificed through cervical dislocation; brains were removed and placed into cold 1× PBS. Biopsy punches of the visual cortex of both hemispheres were taken with a tissue puncher (2.5 mm diameter), and meninges and white matter were carefully removed using forceps to have a tissue sample consisting of gray matter only. Each sample was put into a low-protein binding Eppendorf tube, frozen on dry ice, and stored at −80°C until further processing. Tissue samples were lysed in NP-40 buffer [1% NP-40 in 10 mM tris (pH 7.4) and 150 mM NaCl] in a Precellys homogenizer (VWR), and 10 μg of total protein per sample was proteolyzed with Lys-C and trypsin using a modified FASP (filter-aided sample preparation) procedure.

LC-MS/MS analysis was performed on a Q Exactive HF mass spectrometer (Thermo Fisher Scientific) online coupled to a nano-reverse phase liquid chromatography (RSLC) (Ultimate 3000 RSLC, Dionex) system. Tryptic peptides were accumulated on a nanotrap column (Acclaim PepMap 100 C18; 5 μm, 100 Å, 300 μm inner diameter by 5 mm; Thermo Fisher Scientific) at a flow rate of 30 μl/min and then separated by reversed-phase chromatography (μPAC column; 200 cm length, with pillar array backbone at an interpillar distance of 2.5 μm; PharmaFluidics, Zwijnaarde, Belgium) using a nonlinear gradient for 240 min from 3 to 42% buffer B [acetonitrile/0.1% formic acid (v/v) in high-performance liquid chromatography (HPLC)–grade water] in buffer A [2% acetonitrile/0.1% formic acid (v/v) in HPLC-grade water] at a flow rate of 300 nl/min. MS spectra were recorded at a resolution of 60,000 with an automatic gain control (AGC) target of 3×10^6 and a maximum injection time of 50 ms at a range of 300 to 1500 mass/charge ratio (m/z). From the MS scan, the 10 most abundant ions were selected for higher energy collisional dissociation (HCD) fragmentation with a normalized collision energy of 27, an isolation window of 1.6 m/z, and a dynamic exclusion of 30 s. MS/MS spectra were recorded at a resolution of 15,000 with an AGC target of 105 and a maximum injection time of 50 ms.

Proteome Discoverer 2.4 software (Thermo Fisher Scientific; version 2.4.1.15) was used for peptide and protein identification via a database search (SEQUEST HT search engine) against Swiss-Prot database, taxonomy mouse (17,038 sequences), considering full tryptic specificity, allowing for up to two missed tryptic cleavage sites, precursor mass tolerance of 10 parts per million, and fragment mass tolerance of 0.02 Da. Carbamidomethylation of Cys was set as a static modification. Dynamic modifications included deamidation of Asn and Gln, oxidation of Met, and a combination of Met loss with acetylation on protein N terminus. Percolator (79) was used for validating peptide spectrum matches and peptides, accepting only the top-scoring hit for each spectrum, and satisfying the cutoff values for false discovery rate (FDR) < 1% (high confidence). Protein groups were additionally filtered for an identification FDR <5% (target/decoy concatenated search validation). The final list of proteins complied with the strict parsimony principle.

Data processing—Label-free quantification

Peak intensities (at RT apex) for top three unique peptides were used for pairwise ratio calculations. Abundance values were normalized to the total peptide amount to account for sample load errors. The protein abundances were calculated, summing the abundance values for admissible peptides. The final protein ratio was calculated using median peptide ratios of at least eight biological replicates each (eight replicates WT aged 17 months, 10 replicates transgenic APP/PS1, and 10 replicates WT 8 months controls). P values were

calculated on the basis of the approach described (*80*). Data were filtered to ensure direct identifications (not based on match-between run) in at least 30% of samples within at least one experimental group. To visualize the data, volcano plots with $\log_2$ abundance ratios of sample replicates of each brain condition and the corresponding $\log_{10} P$ values were created with Microsoft Excel. For GO enrichment, significantly differentially expressed proteins were run against a background list of all detected proteins using the webserver GOrilla (http://cbl-gorilla.cs.technion.ac.il/) (*81*).

Statistical analysis

Graphs and statistical analysis were done with GraphPad Prism 5.0 or the abovementioned software. Values are reported as means ± SEM calculated between different mice. Statistical significance was defined as *$P \leq 0.05$, **$P \leq 0.01$, ***$P \leq 0.005$, and ****$P \leq 0.0005$. Normality of data was verified using Shapiro-Wilk test. For variables normally distributed, statistical significance was calculated using one-way analysis of variance (ANOVA) followed by Bonferroni or Holm-Sidak post-test. For all connectivity analyses, Kruskal-Wallis tests were performed followed by Dunn's test for multiple comparison analysis. Statistical significance for the proteomics experiment was ascertained using the approach described by Navarro *et al.* (*80*), which is based on the presumption that we look for expression changes of proteins that are just a few in comparison to the number of total proteins being quantified. The quantification variability of the nonchanging "background" proteins can be used to infer which proteins change their expression in a statistically significant manner. Proteins with $P < 0.05$ were considered significantly changed.

SUPPLEMENTARY MATERIALS

Supplementary material for this article is available at https://science.org/doi/10.1126/sciadv.abg9287

View/request a protocol for this paper from *Bio-protocol*.

REFERENCES AND NOTES

1. R. A. Barker, M. Götz, M. Parmar, New approaches for brain repair—From rescue to reprogramming. *Nature* **557**, 329–334 (2018).
2. S. Grade, M. Götz, Neuronal replacement therapy: Previous achievements and challenges ahead. *NPJ Regen. Med.* **2**, 29 (2017).
3. R. A. Barker, M. Parmar, L. Studer, J. Takahashi, Human trials of stem cell–derived dopamine neurons for Parkinson's disease: Dawn of a new era. *Cell Stem Cell* **21**, 569–573 (2017).
4. V. Tabar, L. Studer, Pluripotent stem cells in regenerative medicine: Challenges and recent progress. *Nat. Rev. Genet.* **15**, 82–92 (2014).
5. L. Studer, V. Tabar, Parkinson's disease grafts benefit from well-timed growth factor. *Nature* **582**, 39–40 (2020).
6. A. Björklund, M. Parmar, Dopamine cell therapy: From cell replacement to circuitry repair. *J. Parkinsons Dis.* **11**, S159–S165 (2021).
7. M. Götz, R. Bocchi, Neuronal replacement: Concepts, achievements, and call for caution. *Curr. Opin. Neurobiol.* **69**, 185–192 (2021).
8. R. A. Barker; TRANSEURO consortium, Designing stem-cell-based dopamine cell replacement trials for Parkinson's disease. *Nat. Med.* **25**, 1045–1053 (2019).
9. J. S. Schweitzer, B. Song, T. M. Herrington, T.-Y. Park, N. Lee, S. Ko, J. Jeon, Y. Cha, K. Kim, Q. Li, C. Henchcliffe, M. Kaplitt, C. Neff, O. Rapalino, H. Seo, I.-H. Lee, J. Kim, T. Kim, G. A. Petsko, J. Ritz, B. M. Cohen, S.-W. Kong, P. Leblanc, B. S. Carter, K.-S. Kim, Personalized iPSC-derived dopamine progenitor cells for Parkinson's disease. *N. Engl. J. Med.* **382**, 1926–1932 (2020).
10. M. Parmar, S. Grealish, C. Henchcliffe, The future of stem cell therapies for Parkinson disease. *Nat. Rev. Neurosci.* **21**, 103–115 (2020).
11. M. Parmar, A. Björklund, From skin to brain: A Parkinson's disease patient transplanted with his own cells. *Cell Stem Cell* **27**, 8–10 (2020).
12. M. Jaber, M. Benoit-Marand, L. Prestoz, A. Gaillard, Cell transplantation in the damaged adult brain. *Rev. Neurol.* **169**, 838–843 (2013).
13. A. Gaillard, M. Jaber, Rewiring the brain with cell transplantation in Parkinson's disease. *Trends Neurosci.* **34**, 124–133 (2011).
14. A. Gaillard, L. Prestoz, B. Dumartin, A. Cantereau, F. Morel, M. Roger, M. Jaber, Reestablishment of damaged adult motor pathways by grafted embryonic cortical neurons. *Nat. Neurosci.* **10**, 1294–1299 (2007).
15. T. V. Wuttke, F. Markopoulos, H. Padmanabhan, A. P. Wheeler, V. N. Murthy, J. D. MacKlis, Developmentally primed cortical neurons maintain fidelity of differentiation and establish appropriate functional connectivity after transplantation. *Nat. Neurosci.* **21**, 517–529 (2018).
16. C. S. Hernit-Grant, J. D. Macklis, Embryonic neurons transplanted to regions of targeted photolytic cell death in adult mouse somatosensory cortex re-form specific callosal projections. *Exp. Neurol.* **139**, 131–142 (1996).
17. I. Espuny-Camacho, K. A. Michelsen, D. Linaro, A. Bilheu, S. Acosta-Verdugo, A. Herpoel, M. Giugliano, A. Gaillard, P. Vanderhaeghen, Human pluripotent stem-cell-derived cortical neurons integrate functionally into the lesioned adult murine visual cortex in an area-specific way. *Cell Rep.* **23**, 2732–2743 (2018).
18. S. Falkner, S. Grade, L. Dimou, K. K. Conzelmann, T. Bonhoeffer, M. Götz, M. Hübener, Transplanted embryonic neurons integrate into adult neocortical circuits. *Nature* **539**, 248–253 (2016).
19. D. Linaro, B. Vermaercke, R. Iwata, A. Ramaswamy, B. Libé-Philippot, L. Boubakar, B. A. Davis, K. Wierda, K. Davie, S. Poovathingal, P. A. Penttila, A. Bilheu, L. de Bruyne, D. Gall, K. K. Conzelmann, V. Bonin, P. Vanderhaeghen, Xenotransplanted human cortical neurons reveal species-specific development and functional integration into mouse visual circuits. *Neuron* **104**, 972–986.e6 (2019).
20. S. Palma-Tortosa, D. Tornero, M. G. Hansen, E. Monni, M. Hajy, S. Kartsivadze, S. Aktay, O. Tsupykov, M. Parmar, K. Deisseroth, G. Skibo, O. Lindvall, Z. Kokaia, Activity in grafted human iPS cell–derived cortical neurons integrated in stroke-injured rat brain regulates motor behavior. *Proc. Natl. Acad. Sci. U.S.A.* **117**, 9094–9100 (2020).
21. M. Xiong, Y. Tao, Q. Gao, B. Feng, W. Yan, Y. Zhou, T. A. Kotsonis, T. Yuan, Z. You, Z. Wu, J. Xi, A. Haberman, J. Graham, J. Block, W. Zhou, Y. Chen, S.-C. Zhang, Human stem cell-derived neurons repair circuits and restore neural function. *Cell Stem Cell* **28**, 112–126.e6 (2021).
22. D. Tornero, O. Tsupykov, M. Granmo, C. Rodriguez, M. Grønning-Hansen, J. Thelin, E. Smozhanik, C. Laterza, S. Wattananit, R. Ge, J. Tatarishvili, S. Grealish, O. Brüstle, G. Skibo, M. Parmar, J. Schouenborg, O. Lindvall, Z. Kokaia, Synaptic inputs from stroke-injured brain to grafted human stem cell-derived neurons activated by sensory stimuli. *Brain* **140**, 692–706 (2017).
23. J. Doerr, M. K. Schwarz, D. Wiedermann, A. Leinhaas, A. Jakobs, F. Schloen, I. Schwarz, M. Diedenhofen, N. C. Braun, P. Koch, D. A. Peterson, U. Kubitscheck, M. Hoehn, O. Brüstle, Whole-brain 3D mapping of human neural transplant innervation. *Nat. Commun.* **8**, 14162 (2017).
24. Q. Xing, A. Lin, Z. Su, C. Liu, W. Huang, W. Guo, G. Pan, Y. Guo, X. Zhong, Retrograde monosynaptic tracing through an engineered human embryonic stem cell line reveals synaptic inputs from host neurons to grafted cells. *Cell Regen.* **8**, 1–8 (2019).
25. A. F. Adler, A. Björklund, M. Parmar, Transsynaptic tracing and its emerging use to assess graft-reconstructed neural circuits. *Stem Cells* **38**, 716–726 (2020).
26. A. F. Adler, T. Cardoso, S. Nolbrant, B. Mattsson, D. B. Hoban, U. Jarl, J. N. Wahlestedt, S. Grealish, A. Björklund, M. Parmar, hESC-derived dopaminergic transplants integrate into basal ganglia circuitry in a preclinical model of Parkinson's disease. *Cell Rep.* **28**, 3462–3473.e5 (2019).
27. R. S. Petralia, M. P. Mattson, P. J. Yao, Communication breakdown: The impact of ageing on synapse structure. *Ageing Res. Rev.* **14**, 31–42 (2014).
28. L. Rajendran, R. C. Paolicelli, Microglia-mediated synapse loss in Alzheimer's disease. *J. Neurosci.* **38**, 2911–2919 (2018).
29. C. M. Henstridge, M. Tzioras, R. C. Paolicelli, Glial contribution to excitatory and inhibitory synapse loss in neurodegeneration. *Front. Cell. Neurosci.* **13**, 63 (2019).
30. J. E. Burda, M. V. Sofroniew, Reactive gliosis and the multicellular response to CNS damage and disease. *Neuron* **81**, 229–248 (2014).
31. N. R. Sims, W. P. Yew, Reactive astrogliosis in stroke: Contributions of astrocytes to recovery of neurological function. *Neurochem. Int.* **107**, 88–103 (2017).
32. R. Radde, T. Bolmont, S. A. Kaeser, J. Coomaraswamy, D. Lindau, J. Stoltze, M. E. Calhoun, F. Jäggi, H. Wolburg, S. Gengler, C. Haass, B. Ghetti, C. Czech, C. Hölscher, P. M. Mathews, M. Jucker, Aβ42-driven cerebral amyloidosis in transgenic mice reveals early and robust pathology. *EMBO Rep.* **7**, 940–946 (2006).
33. S. Sirko, G. Behrendt, P. A. Johansson, P. Tripathi, M. Costa, S. Bek, C. Heinrich, S. Tiedt, D. Colak, M. Dichgans, I. R. Fischer, N. Plesnila, M. Staufenbiel, C. Haass, M. Snapyan, A. Saghatelyan, L. H. Tsai, A. Fischer, K. Grobe, L. Dimou, M. Götz, Reactive glia in the injured brain acquire stem cell properties in response to sonic hedgehog. *Cell Stem Cell* **12**, 426–439 (2013).
34. M. Pekny, U. Wilhelmsson, M. Pekna, The dual role of astrocyte activation and reactive gliosis. *Neurosci. Lett.* **565**, 30–38 (2014).

35. G. Heimann, L. L. Canhos, J. Frik, G. Jäger, T. Lepko, J. Ninkovic, M. Götz, S. Sirko, Changes in the proliferative program limit astrocyte homeostasis in the aged post-traumatic murine cerebral cortex. *Cereb. Cortex* **27**, 4213–4228 (2017).

36. I. Espuny-Camacho, A. M. Arranz, M. Fiers, A. Snellinx, K. Ando, S. Munck, J. Bonnefont, L. Lambot, N. Corthout, L. Omodho, E. Vanden Eynden, E. Radaelli, I. Tesseur, S. Wray, A. Ebneth, J. Hardy, K. Leroy, J. P. Brion, P. Vanderhaeghen, B. de Strooper, Hallmarks of Alzheimer's disease in stem-cell-derived human neurons transplanted into mouse brain. *Neuron* **93**, 1066–1081.e8 (2017).

37. M. Martinez-Losa, T. E. Tracy, K. Ma, L. Verret, A. Clemente-Perez, A. S. Khan, I. Cobos, K. Ho, L. Gan, L. Mucke, M. Alvarez-Dolado, J. J. Palop, Nav1.1-overexpressing interneuron transplants restore brain rhythms and cognition in a mouse model of Alzheimer's disease. *Neuron* **98**, 75–89.e5 (2018).

38. L. M. Tong, B. Djukic, C. Arnold, A. K. Gillespie, S. Y. Yoon, M. M. Wang, O. Zhang, J. Knoferle, J. L. R. Rubenstein, A. Alvarez-Buylla, Y. Huang, Inhibitory interneuron progenitor transplantation restores normal learning and memory in ApoE4 knock-in mice without or with Aβ accumulation. *J. Neurosci.* **34**, 9506–9515 (2014).

39. A. K. Shetty, B. Hattiangady, Grafted subventricular zone neural stem cells display robust engraftment and similar differentiation properties and form new neurogenic niches in the young and aged hippocampus. *Stem Cells Transl. Med.* **5**, 1204–1215 (2016).

40. I. Espuny-Camacho, K. A. Michelsen, D. Gall, D. Linaro, A. Hasche, J. Bonnefont, C. Bali, D. Orduz, A. Bilheu, A. Herpoel, N. Lambert, N. Gaspard, S. Péron, S. N. Schiffmann, M. Giugliano, A. Gaillard, P. Vanderhaeghen, Pyramidal neurons derived from human pluripotent stem cells integrate efficiently into mouse brain circuits in vivo. *Neuron* **77**, 440–456 (2013).

41. G. Lupo, S. Gaetani, E. Cacci, S. Biagioni, R. Negri, Molecular signatures of the aging brain: Finding the links between genes and phenotypes. *Neurotherapeutics* **16**, 543–553 (2019).

42. M. P. Mattson, T. V. Arumugam, Hallmarks of brain aging: Adaptive and pathological modification by metabolic states. *Cell Metab.* **27**, 1176–1199 (2018).

43. R. Mostany, J. E. Anstey, K. L. Crump, B. Maco, G. Knott, C. Portera-Cailliau, Altered synaptic dynamics during normal brain aging. *J. Neurosci.* **33**, 4094–4104 (2013).

44. J. J. Rodríguez-Arellano, V. Parpura, R. Zorec, A. Verkhratsky, Astrocytes in physiological aging and Alzheimer's disease. *Neuroscience* **323**, 170–182 (2016).

45. Y. Hou, X. Dan, M. Babbar, Y. Wei, S. G. Hasselbalch, D. L. Croteau, V. A. Bohr, Ageing as a risk factor for neurodegenerative disease. *Nat. Rev. Neurol.* **15**, 565–581 (2019).

46. L. Crews, E. Masliah, Molecular mechanisms of neurodegeneration in Alzheimer's disease. *Hum. Mol. Genet.* **19**, R12–R20 (2010).

47. N. J. Rupp, B. M. Wegenast-Braun, R. Radde, M. E. Calhoun, M. Jucker, Early onset amyloid lesions lead to severe neuritic abnormalities and local, but not global neuron loss in APPPS1 transgenic mice. *Neurobiol. Aging* **32**, 2324.e1–2324.e6 (2011).

48. T. Bittner, S. Burgold, M. M. Dorostkar, M. Fuhrmann, B. M. Wegenast-Braun, B. Schmidt, H. Kretzschmar, J. Herms, Amyloid plaque formation precedes dendritic spine loss. *Acta Neuropathol.* **124**, 797–807 (2012).

49. F. W. Grillo, S. Song, L. M. Teles-Grilo Ruivo, L. Huang, G. Gao, G. W. Knott, B. MacO, V. Ferretti, D. Thompson, G. E. Little, V. de Paola, Increased axonal bouton dynamics in the aging mouse cortex. *Proc. Natl. Acad. Sci. U.S.A.* **110**, E1514–E1523 (2013).

50. I. R. Wickersham, D. C. Lyon, R. J. O. Barnard, T. Mori, S. Finke, K. K. Conzelmann, J. A. T. Young, E. M. Callaway, Monosynaptic restriction of transsynaptic tracing from single, genetically targeted neurons. *Neuron* **53**, 639–647 (2007).

51. S. W. Oh, J. A. Harris, L. Ng, B. Winslow, N. Cain, S. Mihalas, Q. Wang, C. Lau, L. Kuan, A. M. Henry, M. T. Mortrud, B. Ouellette, T. N. Nguyen, S. A. Sorensen, C. R. Slaughterbeck, W. Wakeman, Y. Li, D. Feng, A. Ho, E. Nicholas, K. E. Hirokawa, P. Bohn, K. M. Joines, H. Peng, M. J. Hawrylycz, J. W. Phillips, J. G. Hohmann, P. Wohnoutka, C. R. Gerfen, C. Koch, A. Bernard, C. Dang, A. R. Jones, H. Zeng, A mesoscale connectome of the mouse brain. *Nature* **508**, 207–214 (2014).

52. B. Zingg, H. Hintiryan, L. Gou, M. Y. Song, M. Bay, M. S. Bienkowski, N. N. Foster, S. Yamashita, I. Bowman, A. W. Toga, H. W. Dong, Neural networks of the mouse neocortex. *Cell* **156**, 1096–1111 (2014).

53. X. Zhang, W. Song, The role of APP and BACE1 trafficking in APP processing and amyloid-β generation. *Alzheimer's Res. Ther.* **5**, 46 (2013).

54. M. Orre, W. Kamphuis, L. M. Osborn, A. H. P. Jansen, L. Kooijman, K. Bossers, E. M. Hol, Isolation of glia from Alzheimer's mice reveals inflammation and dysfunction. *Neurobiol. Aging* **35**, 2746–2760 (2014).

55. L. M. Osborn, W. Kamphuis, W. J. Wadman, E. M. Hol, Astrogliosis: An integral player in the pathogenesis of Alzheimer's disease. *Prog. Neurobiol.* **144**, 121–141 (2016).

56. S. Hong, V. F. Beja-Glasser, B. M. Nfonoyim, A. Frouin, S. Li, S. Ramakrishnan, K. M. Merry, Q. Shi, A. Rosenthal, B. A. Barres, C. A. Lemere, D. J. Selkoe, B. Stevens, Complement and microglia mediate early synapse loss in Alzheimer mouse models. *Science* **352**, 712–716 (2016).

57. J. Presumey, A. R. Bialas, M. C. Carroll, Complement system in neural synapse elimination in development and disease. *Adv. Immunol.* **135**, 53–79 (2017).

58. F. Song, A. Poljak, N. A. Kochan, M. Raftery, H. Brodaty, G. A. Smythe, P. S. Sachdev, Plasma protein profiling of Mild Cognitive Impairment and Alzheimer's disease using iTRAQ quantitative proteomics. *Proteome Sci.* **12**, 1–13 (2014).

59. A. H. Stephan, D. V. Madison, J. M. Mateos, D. A. Fraser, E. A. Lovelett, L. Coutellier, L. Kim, H. H. Tsai, E. J. Huang, D. H. Rowitch, D. S. Berns, A. J. Tenner, M. Shamloo, B. A. Barres, A dramatic increase of C1q protein in the CNS during normal aging. *J. Neurosci.* **33**, 13460–13474 (2013).

60. C. Luchena, J. Zuazo-Ibarra, E. Alberdi, C. Matute, E. Capetillo-Zarate, Contribution of neurons and glial cells to complement-mediated synapse removal during development, aging and in Alzheimer's disease. *Mediators Inflamm.* **2018**, 2530414 (2018).

61. M. A. Busche, A. Konnerth, Impairments of neural circuit function in Alzheimer's disease. *Philos. Trans. R. Soc. B Biol. Sci.* **371**, 20150429 (2016).

62. M. A. Busche, G. Eichhoff, H. Adelsberger, D. Abramowski, K.-H. Wiederhold, C. Haass, M. Staufenbiel, A. Konnerth, O. Garaschuk, Clusters of hyperactive neurons near amyloid plaques in a mouse model of Alzheimer's disease. *Science* **321**, 1686–1689 (2008).

63. M. Bergami, G. Masserdotti, S. G. Temprana, E. Motori, T. M. Eriksson, J. Göbel, S. M. Yang, K.-K. Conzelmann, A. F. Schinder, M. Götz, B. Berninger, A critical period for experience-dependent remodeling of adult-born neuron connectivity. *Neuron* **85**, 710–717 (2015).

64. S. N. Burke, C. A. Barnes, Neural plasticity in the ageing brain. *Nat. Rev. Neurosci.* **7**, 30–40 (2006).

65. M. Jucker, L. Bondolfi, M. E. Calhoun, J. M. Long, D. K. Ingram, Structural brain aging in inbred mice: Potential for genetic linkage. *Exp. Gerontol.* **35**, 1383–1388 (2000).

66. J. D. Whitesell, A. R. Buckley, J. E. Knox, L. Kuan, N. Graddis, A. Pelos, A. Mukora, W. Wakeman, P. Bohn, A. Ho, K. E. Hirokawa, J. A. Harris, Whole brain imaging reveals distinct spatial patterns of amyloid beta deposition in three mouse models of Alzheimer's disease. *J. Comp. Neurol.* **527**, 2122–2145 (2019).

67. B. Stevens, N. J. Allen, L. E. Vazquez, G. R. Howell, K. S. Christopherson, N. Nouri, K. D. Micheva, A. K. Mehalow, A. D. Huberman, B. Stafford, A. Sher, A. M. M. Litke, J. D. Lambris, S. J. Smith, S. W. M. John, B. A. Barres, The classical complement cascade mediates CNS synapse elimination. *Cell* **131**, 1164–1178 (2007).

68. A. H. Stephan, B. A. Barres, B. Stevens, The complement system: An unexpected role in synaptic pruning during development and disease. *Annu. Rev. Neurosci.* **35**, 369–389 (2012).

69. B. A. Györffy, V. Tóth, G. Török, P. Gulyássy, A. Kovács, H. Vadászi, A. Micsonai, M. E. Tóth, M. Sántha, L. Homolya, L. Drahos, G. Juhász, K. A. Kékesi, J. Kardos, Synaptic mitochondrial dysfunction and septin accumulation are linked to complement-mediated synapse loss in an Alzheimer's disease animal model. *Cell. Mol. Life Sci.* **77**, 5243–5258 (2020).

70. M. I. Fonseca, J. Zhou, M. Botto, A. J. Tenner, Absence of C1q leads to less neuropathology in transgenic mouse models of Alzheimer's disease. *J. Neurosci.* **24**, 6457–6465 (2004).

71. D. Datta, S. N. Leslie, Y. M. Morozov, A. Duque, P. Rakic, C. H. van Dyck, A. C. Nairn, A. F. T. Arnsten, Classical complement cascade initiating C1q protein within neurons in the aged rhesus macaque dorsolateral prefrontal cortex. *J. Neuroinflammation* **17**, 8 (2020).

72. T. Toda, F. H. Gage, Review: Adult neurogenesis contributes to hippocampal plasticity. *Cell Tissue Res.* **373**, 693–709 (2018).

73. N. Toni, E. M. Teng, E. A. Bushong, J. B. Aimone, C. Zhao, A. Consiglio, H. van Praag, M. E. Martone, M. H. Ellisman, F. H. Gage, Synapse formation on neurons born in the adult hippocampus. *Nat. Neurosci.* **10**, 727–734 (2007).

74. A. Tashiro, V. M. Sandler, N. Toni, C. Zhao, F. H. Gage, NMDA-receptor-mediated, cell-specific integration of new neurons in adult dentate gyrus. *Nature* **442**, 929–933 (2006).

75. S. Grade, J. Thomas, Y. Zarb, M. Thorwirth, K.-K. Conzelmann, S. M. Hauck, M. Götz, Brain injury environment critically influences the connectivity of transplanted neurons. *Sci. Adv.* **8**, eabg9445 (2022).

76. J. Takatoh, A. Nelson, X. Zhou, M. M. L. Bolton, M. D. Ehlers, B. R. Arenkiel, R. Mooney, F. Wang, New modules are added to vibrissal premotor circuitry with the emergence of exploratory whisking. *Neuron* **77**, 346–360 (2013).

77. T. Nakamura, M. C. Colbert, J. Robbins, Neural crest cells retain multipotential characteristics in the developing valves and label the cardiac conduction system. *Circ. Res.* **98**, 1547–1554 (2006).

78. T. Iwasato, A. Datwani, A. M. Wolf, H. Nishiyama, Y. Taguchi, T. Knöpfel, R. S. Erzurumlu, S. Itohara, Cortex-restricted disruption of NMDAR1 impairs neuronal patterns in the barrel cortex. *Nature* **406**, 726–731 (2000).

79. L. Käll, J. D. Canterbury, J. Weston, W. S. Noble, M. J. MacCoss, Semi-supervised learning for peptide identification from shotgun proteomics datasets. *Nat. Methods* **4**, 923–925 (2007).

80. P. Navarro, M. Trevisan-Herraz, E. Bonzon-Kulichenko, E. Núñez, P. Martínez-Acedo, D. Pérez-Hernández, I. Jorge, R. Mesa, E. Calvo, M. Carrascal, M. L. Hernáez, F. García, J. A. Bárcena, K. Ashman, J. Abian, C. Gil, J. M. Redondo, J. Vázquez, General statistical

framework for quantitative proteomics by stable isotope labeling. *J. Proteome Res.* **13**, 1234–1247 (2014).

81. E. Eden, R. Navon, I. Steinfeld, D. Lipson, Z. Yakhini, *GOrilla*: A tool for discovery and visualization of enriched GO terms in ranked gene lists. *BMC Bioinformatics* **10**, 48 (2009).

82. Y. Perez-Riverol, A. Csordas, J. Bai, M. Bernal-Llinares, S. Hewapathirana, D. J. Kundu, A. Inuganti, J. Griss, G. Mayer, M. Eisenacher, E. Pérez, J. Uszkoreit, J. Pfeuffer, T. Sachsenberg, Ş. Yilmaz, S. Tiwary, J. Cox, E. Audain, M. Walzer, A. F. Jarnuczak, T. Ternent, A. Brazma, J. A. Vizcaíno, The PRIDE database and related tools and resources in 2019: Improving support for quantification data. *Nucleic Acids Res.* **47**, D442–D450 (2019).

Science Advances

Excessive local host-graft connectivity in aging and amyloid-loaded brain

Judith Thomas, Maria Fernanda Martinez-Reza, Manja Thorwirth, Yvette Zarb, Karl-Klaus Conzelmann, Stefanie M. Hauck, Sofia Grade, and Magdalena Gtz

View the article online
https://www.science.org/doi/10.1126/sciadv.abg9287
Permissions
https://www.science.org/help/reprints-and-permissions

Use of this article is subject to the Terms of service